

# Learning to Predict the 3D Layout of a Scene

Jihao Andreas Lin      Jakob Brünker      Daniel Fährmann

Department of Computer Science, TU Darmstadt

## Abstract

While 2D object detection has improved significantly over the past years [1, 2, 3, 4, 5, 6], real world applications of computer vision often require an understanding of the 3D layout of a scene. Many recent approaches to 3D detection [7, 8, 9, 10] use LiDAR point clouds for prediction. We propose a method that only uses a single RGB image, thus enabling applications in devices or vehicles that do not have LiDAR sensors. By using an RGB image, we can leverage the maturity and success of recent 2D object detectors, by extending a 2D detector with a 3D detection head. In this paper we discuss different approaches and experiments, including both regression and classification methods, for designing this 3D detection head. Furthermore, we evaluate how subproblems and implementation details impact the overall prediction result. We use the KITTI [11] dataset for training, which consists of street traffic scenes with class labels, 2D bounding boxes and 3D annotations with seven degrees of freedom. Our final architecture is based on Faster R-CNN [3]. The outputs of the convolutional backbone are fixed sized feature maps for every region of interest. Fully connected layers within the network head then propose an object class and perform 2D bounding box regression. We extend the network head by a 3D detection head, which predicts every degree of freedom of a 3D bounding box via classification. We achieve a mean average precision of 47.3% for moderately difficult data, measured at a 3D intersection over union threshold of 70%, as required by the official KITTI benchmark; outperforming previous state-of-the-art single RGB only methods by a large margin.

## 1. Introduction

Over the past years, 2D detectors have matured and achieved excellent results. We leverage this maturity by extending a state-of-the-art 2D detector to a 3D detector that only relies on a single RGB image. We use the KITTI [11] dataset that consists of 3D annotated traffic scenes.

In contrast to the four degrees of freedom of a 2D bound-

ing box, a 3D bounding box has nine degrees of freedom. These can be separated into three parts with three degrees of freedom each: dimensions, location and orientation. We will refer to the dimensions as height, width and length and to the location as x, y and z. The 3D annotations of the KITTI [11] dataset only provide seven degrees of freedom because they only provide one value for the orientation. We will refer to this orientation as angle.

The problem of 3D detection is very ill-posed when lacking depth information. The scale, which we will also refer to as the depth versus size ambiguity, is a common problem: An object that is far away but big in size appears identical in an image as an object that is close to the camera but small in size. Many recent approaches to 3D detection, such as *PointFusion* [7], *AVOD* [8], *VoxelNet* [9] and *F-PointNet* [10] use LiDAR point clouds as their source of depth information, but we do not. There is also no possibility of exploiting binocular depth cues because we only use a single RGB image. However, this makes our method more feasible for smaller devices, such as smartphones, that have neither stereo cameras nor LiDAR sensors.

In this paper we evaluate different state-of-the-art 2D detectors by debating their suitability as a backbone for our 3D detection task. We then present different approaches to 3D detection, including regression, classification and human pose estimation inspired methods with explanations about incorporating information from the 2D detector and unobvious problems in orientation and depth prediction. Finally, we discuss their capabilities, problems, implementation details and detection performance. Our evaluation shows how different subproblems contribute to the final result and how implementation details can significantly impact the prediction accuracy.

For our experiments we use the *Faster R-CNN* [3] architecture with a *ResNet-101* [12] convolutional backbone for generating feature maps, region proposals, 2D bounding boxes and object classification. We replace the *RoIPool* layer with the *RoIAlign* layer proposed in *Mask R-CNN* [4] for more precise local feature extraction.

## 2. Related Work

### 2.1. 2D Object Detection

#### 2.1.1 Faster R-CNN

The Faster R-CNN [3] architecture uses a deep convolutional network like *ResNet* [12] to compute a feature map for the entire image. A *Region Proposal Network* generates regions of interest, that are then used to create a fixed sized crop of the feature map for every instance proposal by applying the *RoIPool* layer proposed in [3]. These cropped feature maps are then used to regress the 2D bounding box and classify the corresponding instance.

We use *Faster R-CNN* as our baseline 2D detector. We extend the network head to allow 3D detection.

#### 2.1.2 Mask R-CNN

As an extension to *Faster R-CNN* [3], the *Mask R-CNN* [4] architecture consists of the same underlying structure. However, a feature pyramid network [13] is used to obtain feature maps for various scales. Instead of just detecting object class and 2D bounding boxes, *Mask R-CNN* addresses the task of instance segmentation, in which every object has to be labeled with pixel-wise accuracy.

One implementation difference is the method of extracting local feature maps. The *Mask R-CNN* paper introduces a *RoIAlign* layer which is used instead of the *RoIPool* layer.

While *RoIPool* performs coarse spatial quantization by rounding coordinates of region proposals to integer values, *RoIAlign* generates the fixed size feature maps by using bilinear interpolation of the feature map values, thus generating more precise feature maps and overall results. According to [4], this seemingly small difference has a significant impact on their results for instance segmentation.

*Mask R-CNN* uses an additional network head to predict the instance segmentation by generating a segmentation mask for every object. This network head consists of multiple convolutional layers and is trained with binary cross entropy loss, where every pixel inside a region of interest is classified as either belonging to the object or being part of the background. For implementation details, please see [4].

Our *Keypoints* approach makes use of the instance segmentation capabilities of *Mask R-CNN*.

#### 2.1.3 YOLO9000

Another state-of-the-art 2D detector that offers real-time performance and a vast amount of different object classes, *YOLO9000* [5] claims to outperform *Faster R-CNN* [3] in terms of mean average precision, while also running at 40 FPS. The extremely fast inference is obtained by making use of a one-stage network architecture: *YOLO9000* is not split into a network backbone for computing feature maps

and network heads to infer object classes and bounding boxes, but instead consists of a single convolutional network. This network, called *Darknet-19*, accomplishes feature extraction, region proposal, classification and bounding box prediction all by itself; it consists of only 19 layers, thus running significantly faster than *ResNet* [12] based backbones.

Although *YOLO9000* [5] seems to offer more than other 2D detectors, we eventually decided not to use their architecture due to several reasons: Fast real-time performance is not our main objective, this advantage is not significant for our research. Being a one-stage detector, we expected that the underlying *Darknet-19* lacks extendibility for our purposes of 3D detection. The network is specifically engineered for the task of 2D detection and thus very compact and hard to modify. It would still be possible to extract the features from the last convolutional layer and feed them to an additional network head, but while the features generated by this comparatively shallow network suffice for 2D detection, we are skeptical about the feature representation being deep enough for 3D detection.

#### 2.1.4 RetinaNet

Like *YOLO9000*, *RetinaNet* [6] is a one-stage detector. The paper examines why this type of detector had so far not matched the accuracy of two-stage detectors, and concludes that the problem is imbalance between foreground classes and the background class. To alleviate this problem, they introduce a new loss function, called *Focal Loss*, which focuses training on hard examples while reducing the importance of easy examples that are already well-classified.

The backbone architecture of *RetinaNet* is similar to that of *Faster R-CNN*, also using *ResNet* [12], but instead of a region proposal network, the features are directly fed into two subnetworks. The first predicts a class for anchor boxes, and the second is trained to regress from anchor boxes to ground-truth boxes.

Using this architecture, *RetinaNet* surpasses existing state-of-the-art methods in average precision, while also being faster.

Although we considered using *RetinaNet* for our task, we ended up not using it. As with *YOLO9000*, we expected that *RetinaNet* would be harder to extend and adjust to our specific needs due to it being a one-stage detector.

## 2.2. 3D Object Detection

### 2.2.1 F-PointNet

Recent 3D detectors such as *PointFusion* [7], *AVOD* [8], *VoxelNet* [9] and *F-PointNet* [10] rely on LiDAR data. Currently, *F-PointNet* achieves the highest 3D detection precision; their method involves a large network that can be split into 3 different parts.

The first part is a 2D detector, such as *Faster R-CNN* [3], that generates 2D region proposals and classifies the objects. They extend these region proposals to 3D frustum proposals by considering arbitrary depth of the object. All LiDAR points inside a frustum are then sampled to create a point cloud for every proposal.

These point clouds are passed to the second part of the network, which is an adaptation of *PointNet* [14, 15]. It carries out 3D instance segmentation by binary classification of every point of the point cloud to either belong to the object or background. The results of this step are segmented object points for every frustum proposal.

The last step is estimating the amodal 3D bounding boxes. Segmented object points are given as input to a *light-weight regression PointNet*, called *T-Net*. It translates segmented points to align their centroids with bounding box centers. Finally, 3D boxes are estimated with another *PointNet*. For details, see [10].

We cannot adapt *F-PointNet* for our task, since we do not use LiDAR data. Nonetheless, becoming familiar with a state-of-the-art 3D detector, that uses LiDAR data, helped us to grasp the complexity and caveats of the task. An example is the depth versus size ambiguity, which we have to address. It also confirms that extending deep CNN based 2D detectors with 3D detection utility is reasonable and produces good results.

### 2.3. Depth Estimation

For our task of 3D detection it is necessary to predict the depth of detected objects. Although we only need a depth value for each object, we investigated methods that perform dense monocular depth estimation for the purpose of potentially adapting these methods.

The work of Eigen *et al.* [16] is a common baseline in this field. They use two convolutional networks: The first predicts a coarse depth map of the input image. The coarse result is then used by the second network to predict a refined result. While their results on the indoor NYU [17] dataset are good, they point out that their method does not work very well for KITTI [11] images. Adapting the model architecture of Eigen *et al.* [16] for our purpose is not very feasible. Instead of two additional convolutional networks and having to use outputs as inputs, we would prefer to have an architecture that can directly make use of the features computed by the 2D detector.

At this point we investigated the method of Li and He *et al.* [19]. They use a single convolutional network to estimate monocular dense depth of RGB images. The main emphasis of their model architecture lies on the usage of dilated convolution [20] and weighted sum inference.

Dilated convolutions are used to increase the receptive field of neurons, so that they are able to incorporate global and local depth cues. This is similar to refining a coarse



Figure 1. Corner points of a ground truth 3D bounding box.

prediction, which represents global depth cues, by passing it through another network that produces a more precise result, exploiting local depth cues.

In [19], the problem of depth estimation is formulated as a classification task. A fixed number of bins is used, each representing an interval of depth. The depth is estimated by classifying the correct bin. A continuous output depth value is computed by using a weighted sum, i.e. multiplying the estimated score, or confidence, with the corresponding bin value and then summing over all bins.

While we did not implement dilated convolutions, we ended up formulating not just the depth estimation, but rather all parameter predictions as classification tasks, which was inspired by Li and He *et al.* [21]. It turned out that training our problem as a classification task yielded better results than regression approaches. In section 3.3 on page 5, we will discuss our usage of bin classification in the context of 3D detection and propose improvements based on the method of Li and He *et al.* [19].

## 3. Approaches

### 3.1. Keypoints

Inspired by the human pose estimation capabilities of *Mask R-CNN* [4], our initial approach consisted of adapting these. Instead of predicting the position of a human shoulder or leg, we would predict the 8 corner points of a 3D bounding box, treating their image coordinates as 16 degrees of freedom.

However, we soon encountered severe problems with this approach: We assume 3D bounding boxes are cuboids, but the result of 8 predicted pixels will most likely not be a cuboid, because there are significantly more degrees of freedom than our desired bounding box has. If we encode every corner point as a pair of image coordinates, 8 corner points would already equal 16 degrees of freedom. We considered using 4 corner points, which would result in 8 degrees of freedom, and using the geometry of a cuboid to determine the rest. This would guarantee that the predicted shape is, if not a cuboid, at least a parallelepiped instead of an arbitrary three-dimensional shape with 8 corner points. But even if we assume that our network is capable of perfectly predict-

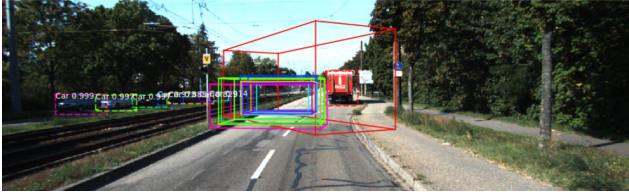


Figure 2. Naïve Regression confirms proposed problems.



Figure 3. Our results after initial improvements.

ing the corner points, there is still another unknown degree of freedom to solve the depth versus size ambiguity. To obtain the final results we would have to transform the corner points, which reside in 2D image coordinates, to 3D camera coordinates by using the camera calibration matrix and the predicted depth.

We realized that this approach is flawed, because it neither solves the task of estimating the depth of an object nor does it make use of constraints which the problem implicitly has.

## 3.2. Regression

### 3.2.1 Naïve Regression

The most naïve way of predicting a 3D bounding box is using a single fully connected layer for every degree of freedom. These layers receive a fixed sized feature map for every proposed object. The feature maps are created by *RoIAlign* [4] and correspond to the regions of interest, predicted by the 2D detector.

This naïve method has several problems: While the network may be able to predict the depth of an object, it cannot predict the  $x$  and  $y$  coordinates of an object, because the local feature map is the only input for the layers that are supposed to predict  $x$  and  $y$ . It does not contain any information about where these features reside in the image. The network is not able to distinguish between two occurrences of similar objects, because their feature representations do not depend on their locations, due to convolutional layers using the same weights at every input location. Therefore, the network cannot correctly predict  $x$  or  $y$  coordinates. We address this problem in the other approaches by using information from the 2D detector. Also, training might take very long if the network is supposed to directly output predictions for the dimensions of objects, because it will have to learn the mean as its bias.

Although we were aware of these problems beforehand, we still decided to do the experiments, both to confirm that



Figure 4. Comparison of the 2D bounding box center (red) and the 3D bounding box center, projected into image space (blue).

our theories are correct and to have a starting point for further improvement.

Our experiments confirmed the expected problems, see figure 2: The objects are all centered in the  $x$ - $y$  plane because the detector cannot predict the correct location by only using local features.

### 3.2.2 Initial Improvements

After our naïve approach indeed showed the previously proposed problems, we constrained the regression approach by implementing prior knowledge of the data, pinhole camera geometry and 2D detector information.

Instead of directly learning the dimensions of objects, the model learns the difference to the mean. This change has no impact on the potential of the neural network, because it is just an offset to the bias of the fully connected layer. However, removing the necessity of learning this bias yields more precise results after the same amount of training time.

Investigation of the ground truth data indicates that the center point of a 2D region of interest is close to the image coordinates of the projected 3D center point (see figure 4). We introduce a method to predict the projected 3D center of an object by learning an offset, denoted by  $du$  and  $dv$ , to the region of interest center predicted by the 2D detector, denoted with image coordinates  $u$  and  $v$ .

Using the predicted depth value and the camera intrinsics, we can then transform the estimated 3D center projection back into camera space to obtain the final 3D coordinates. See the supplementary material for the equations.

### 3.2.3 Constrained Regression

We attempted to implement the approach introduced by Mousavian *et al.* [22]. 2D bounding boxes around objects are generated using a conventional 2D detector, which the model receives as input. The paper assumes that these 2D bounding boxes contain the projected 3D bounding boxes, rather than the projected objects themselves. This approximation is accurate enough for most objects.

Under this assumption, each edge of the 2D bounding box must touch at least one corner of the projected 3D

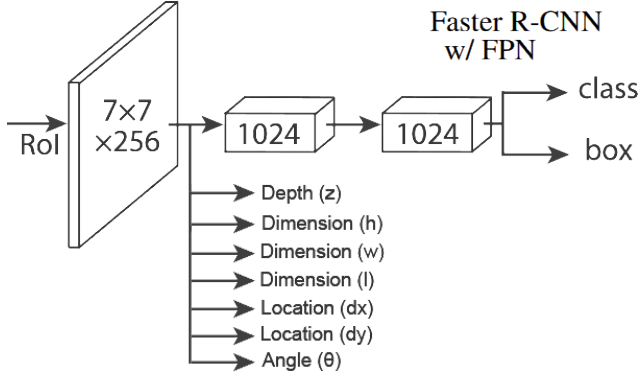


Figure 5. We extended the head architecture of Faster R-CNN. Fully connected layers that predict the degrees of freedom of a 3D bounding box are added. The figure is a modified version of the figure contained in the original *Mask R-CNN* [4] paper.

bounding box. Since this constrains the horizontal coordinates of two corners and the vertical coordinates of two others, it provides four degrees of freedom. As the KITTI dataset provides seven (cf. Introduction), the network has to learn at least three more.

The degrees of freedom that are still learned are the dimensions and the angle. In our implementation the model that predicts these is built out of linear layers, as described in the paper. These layers receive the features produced by *Mask R-CNN* [4] as input. This is different from the original paper, which uses features from a pre-trained *VGG* network [23].

Using the 2D bounding boxes and learned degrees of freedom in combination with the camera intrinsics, it is possible to estimate the translation of the 3D bounding box. An explanation of how this is done can be found in the supplementary material.

The original paper explains that there is a total of 64 possibilities for which corner points touch which edges of the 2D bounding box. The correct solution can only be found when using the correct configuration out of these 64. Unfortunately, the paper does not explain how the correct configuration can be identified. Since we could not overcome this problem, we ultimately abandoned this approach.

### 3.3. Classification

Due to the issues we were facing with regression, we decided to reinterpret our task as a classification problem, because we believe these to train better. Our network head still uses fully connected layers that receive the local feature maps from the underlying 2D detector as input. We are just changing the dimensions and reinterpreting the output of these fully connected layers. The complete architecture is illustrated in figure 5.

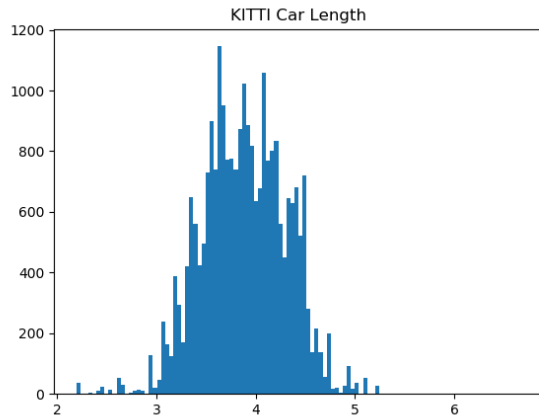


Figure 6. After evaluating this ground truth training data histogram, we decided to use 10 bins ranging from 3.0m to 5.0m with a step size of 0.2m for estimating the length of a car.

#### 3.3.1 Bin Representation

We clamped and quantized the parameters, that are to be predicted, into bins. Every bin represents a possible range of values that a predicted parameter may assume. Our network then learns to classify the correct bin for every degree of freedom using the input feature map.

We choose the range for a degree of freedom by evaluating its histogram distribution, aiming to represent more than 99% of the training data with our chosen clamped (and thus finite) range while also keeping it as small as possible. Choosing a small range constrains the prediction and increases generalizability.

After we determined the range for a degree of freedom, we chose a suitable number of bins, depending on the variance of the training data and our estimate of the generalizability. While intuition suggests that a higher number of bins yields a more precise prediction, choosing a very high number of bins, i.e. number of classes, lowers generalizability because the range of individual bins, i.e. the step size, is decreased and thus fewer training examples are available for each bin. The goal is to choose a number of bins that is low enough so that the network can learn to classify correctly, but also high enough to yield a reasonably precise prediction.

The final result is obtained by computing the weighted sum over all bins. *lower\_bound* is the smallest assumable value of the corresponding parameter.

$$prediction = lower\_bound + \sum_{i=0}^{N-1} score_i \cdot bin\_value_i$$

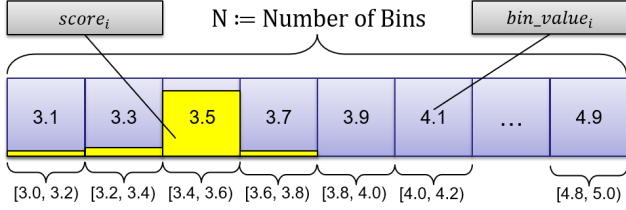


Figure 7. Visual representation of bins used for estimating length. All numbers are in meters. The yellow areas represent the output of a fully connected layer. The *lower\_bound* in this case is 3m.

### 3.3.2 Dimensions

We use three distinct fully connected layers to predict the height, width and length of an object. For the height and width of cars we use 1.2m as lower bound and 2.0m as upper bound with 8 equally distributed bins of step size 0.1m. That means that e.g. the first bin corresponds to the range [1.2m, 1.3m) and has bin value 1.25m. For the length of cars we use 3.0m and 5.0m as lower and upper bound with 10 equally distributed bins of step size 0.2m

### 3.3.3 Depth

After evaluating the training data, we initially decided to use 100 bins and a range of [0m, 100m), with a constant step-size of 1m per bin.

However, changing the depth of an object from 1m to 2m significantly impacts its appearance, while a change from 99m to 100m may not even be noticeable in the image, even though the absolute change is identical. This effect happens due to perspective projection. Estimating absolute depth is easy if an object is close to the camera, but becomes increasingly difficult as the depth increases.

Hence we decided to linearly increase the step-size as the bins represent higher depth values. We believe that such a distribution of bins utilizes the information in the image better than equally distributed bins and enables the network to predict the absolute depth of close objects accurately. At the same time, larger bins for high depth values increase trainability. (cf. section 3.3.1 on the preceding page)

We use 100 bins and a range of [0m, 99m). The first bin has step-size 0.02m, increasing linearly by 0.02m with every bin. Our first bin covers depth values of [0, 0.02m), the second bin covers [0.02m, 0.06m), the third bin covers [0.06m, 0.12m), and so on.

### 3.3.4 X and Y Location

Using the predicted depth and the mathematics of perspective projection, we can now estimate the x and y coordinates.

Similar to how we used  $du$  and  $dv$  in section 3.2.2 on page 4, we now use offsets  $dx$  and  $dy$  in 3D camera coordinates.

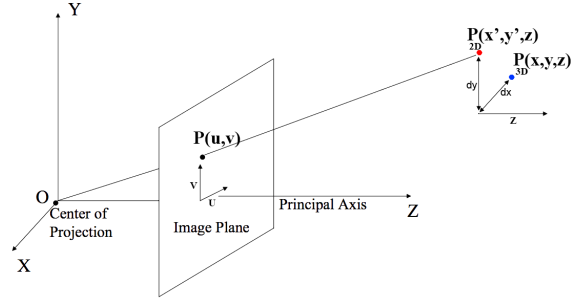


Figure 8. To obtain the 2D region of interest center in 3D camera coordinates, it is put at the same depth as the predicted depth of the object. The  $x'$  and  $y'$  coordinates are then calculated using the intrinsic camera matrix.

First, we transform the 2D region of interest center  $(u, v)$  into camera coordinates  $(x', y', z)$ , using the predicted depth.  $dx$  and  $dy$  are the differences between this transformed region of interest center and the actual 3D object center (see figure 8).

The effect of  $dx$  and  $dy$  on the predicted 3D center is explained in the supplementary material.

For  $dx$  we use 40 bins with a range of [-1m, 1m). In the case  $dy$  we use 20 bins with a range of [-0.5m, 0.5m). Both use a constant step-size of 0.05m.

### 3.3.5 Orientation

Since we use the KITTI dataset, we only have to predict a single angle of orientation. We use 36 bins for this, each representing 10 degrees.

While this is just as simple as the bin representation for the dimensions, training these bins is slightly more complex. The ground truth data has to be pre-processed to make training easier. Why this is the case is explained in [22], and is illustrated in figure 9 on the next page. If one only observes the image patch around the car, as our model does, it looks almost like the car is rotating while it is moving further away. Therefore, it is easier to learn the correct orientation angle if this is taken into account.

The way this is handled can be seen in figure 10 on the following page. While typically, one would use the angle with respect to a line perpendicular to the camera plane, we instead take the angle with respect to a line connecting the camera center and the object center.

### 3.3.6 Implementation Details

Our implementation is based on the Mask R-CNN architecture built by *Matterport* [24]. This architecture contains a *Feature Pyramid Network (FPN)* and a *ResNet101* [12] backbone. Before the image is processed, the mean RGB



Figure 9. The car appears to rotate as it moves further from the camera. Source: Mousavian *et al.* [22]

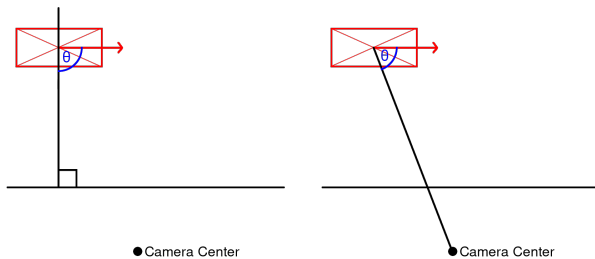


Figure 10. Instead of measuring the angle relative to a line perpendicular to the image plane, the angle is measured relative to a line through the camera center and the object center

values are subtracted from every pixel. A region proposal network then creates 256 anchors using anchor scales (Length of square anchor side in pixels) of 32, 64, 128, 256, 512, anchor ratios (width/height) of 0.5, 1, 2 and an anchor stride of 2. The strides of each layer of the *FPN* are 4, 8, 16, 32, 64. These values are based on a *ResNet101* backbone. The number of regions of interest per image that are fed to the classifier heads is set to 128. A minimum confidence of 0.7 is required to accept a detected instance. We extend the network head architecture to include fully connected layer branches, which predict every degree of freedom via classification. The input dimensionality of each branch corresponds to the  $7 \times 7 \times 256$  features as computed by the *RoIAlign* layer. The output dimensionality in each branch corresponds to the number of bins for every degree of freedom. A softmax activation layer is used to predict the score for each bin. The model trains using stochastic gradient descent optimization with a learning rate of 0.002, momentum of 0.9 and weight decay regularization of 0.0001. The losses of each degree of freedom are defined separately and penalized by a L2 regularization term. All losses contribute evenly.

	Min. BBH	Max. OL	Max. T.
Easy	40 Px	Fully Visible	15%
Moderate	25 Px	Partially Occluded	30%
Hard	25 Px	Difficult to see	50%

Table 1. The requirements for various difficulties according to the KITTI benchmark. These are taken from [25]. The abbreviations mean “bounding box height” (BBH), “occlusion level” (OL) and “truncation” (T).

mAP @ 70% IoU	
Easy	55.0%
Moderate	47.3%
Hard	44.9%

Table 2. The mean average precisions for the difficulties defined for the KITTI benchmark [25]. They are measured for cars, where the intersection over union for the 3D bounding boxes is at least 70%.

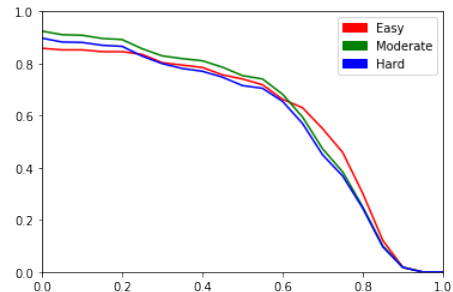


Figure 11. The average precision for various difficulties, evaluated for a range of IoU thresholds between 0% and 100%.

## 4. Evaluation

Our evaluation is done in accordance with the official KITTI 3D object detection benchmark evaluations, which are accessible on the KITTI website [25].

For this evaluation, different difficulties are defined, which specify the objects that are taken into account. The definitions can be seen in table 1. The models are ranked based on the results achieved with moderate difficulty.

The best model listed is *F-PointNet* [10], which achieves an average precision of 70.39% at moderate difficulty. However, this model relies on point clouds from a Velodyne laser scanner, which our method does not use. Among the models not using point clouds, the best model in the list is *3dSSD* [26], which has an average precision of 14.97% at moderate difficulty. However, this method emphasizes speed over accuracy.

The average precision our model achieves at the various difficulties can be seen in table 2. The following evaluations were all made on the whole dataset, including all difficulties. Figures 12 through 16 show how our model performs under various conditions and with various changes. The orange curve always shows the mean average precision of the final model.

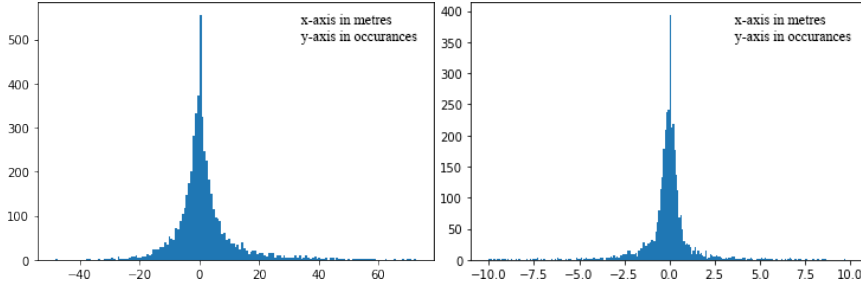


Figure 12. Histograms of the difference between ground truth depth and predicted depth. Left: Naïve approach. Right: Final method. Note the x-axis scale!

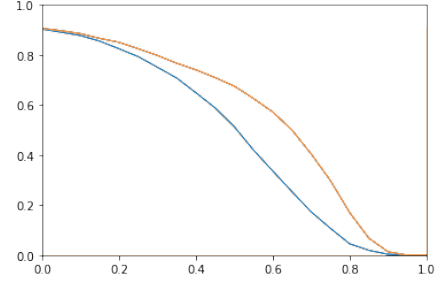


Figure 13. Using the central value of a bin (final model) versus using the smallest value of a bin as *bin\_value*.

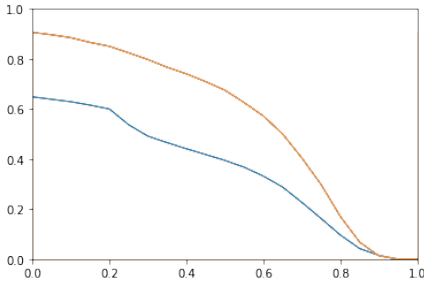


Figure 14. Versus assuming fixed orientation.

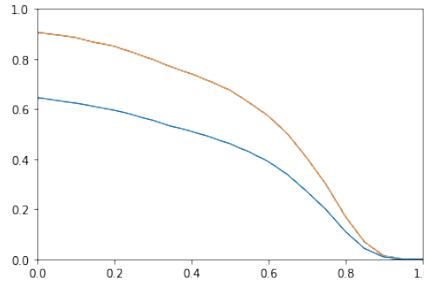


Figure 15. Versus not taking into account  $dx$  and  $dy$ , which were described in section 3.3.4 on page 6.

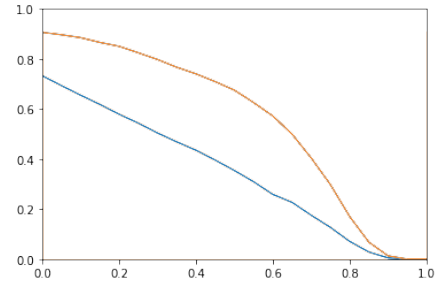


Figure 16. Versus using 100 bins with a constant step-size of 1m for depth prediction.

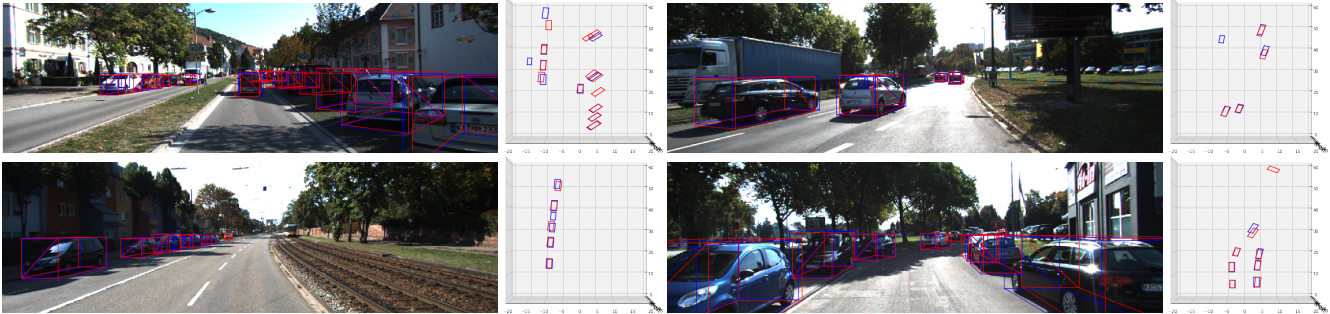


Figure 17. Example results of our final model. The ground truth is displayed in blue, our prediction in red. On the left-hand side is the RGB image, on the right-hand side is a corresponding bird's-eye view.

## 5. Conclusion

Many state-of-the-art 3D detection methods use LiDAR data for their prediction. We have shown that only using a single RGB image for 3D prediction can achieve high accuracy despite lacking important depth cues. Our experiments confirm that reformulating a regression problem as a classification task can significantly improve the results.

Our discarded human pose estimation inspired approach as described in section 3.1 on page 3 does not properly address the problem of depth estimation.

Experiments confirm that our Naïve Regression cannot correctly predict the location of an object by only using local features.

Constrained Regression as introduced by Mousavian *et*

*al.* [22] seems very promising, but we were not able to replicate the results.

Our Classification approach discretizes the search space into bins to predict the degrees of freedom with state-of-the-art accuracy. Using linearly increasing bin sizes turned out to significantly improve depth estimation results.

It should be noted that our model is constrained by the chosen bin hyperparameters and may perform worse in significantly different traffic or non-traffic scenes. This problem could be addressed by finetuning hyperparameters and using more varied training data.

Nonetheless, our final model successfully learned to predict the 3D layout of KITTI traffic scenes without relying on LiDAR data or stereo cues.



## References

- [1] R. B. Girshick, J. Donahue, T. Darrell, and J. Malik, "Rich feature hierarchies for accurate object detection and semantic segmentation," *CoRR*, vol. abs/1311.2524, 2013.
- [2] R. B. Girshick, "Fast R-CNN," *CoRR*, vol. abs/1504.08083, 2015.
- [3] S. Ren, K. He, R. B. Girshick, and J. Sun, "Faster R-CNN: towards real-time object detection with region proposal networks," *CoRR*, vol. abs/1506.01497, 2015.
- [4] K. He, G. Gkioxari, P. Dollár, and R. B. Girshick, "Mask R-CNN," *CoRR*, vol. abs/1703.06870, 2017.
- [5] J. Redmon and A. Farhadi, "YOLO9000: better, faster, stronger," *CoRR*, vol. abs/1612.08242, 2016.
- [6] T. Lin, P. Goyal, R. B. Girshick, K. He, and P. Dollár, "Focal loss for dense object detection," *CoRR*, vol. abs/1708.02002, 2017.
- [7] D. Xu, D. Anguelov, and A. Jain, "Pointfusion: Deep sensor fusion for 3d bounding box estimation," *CoRR*, vol. abs/1711.10871, 2017.
- [8] J. Ku, M. Mozifian, J. Lee, A. Harakeh, and S. Waslander, "Joint 3d proposal generation and object detection from view aggregation," *CoRR*, vol. abs/1712.022.94, 2017.
- [9] Y. Zhou and O. Tuzel, "Voxelnet: End-to-end learning for point cloud based 3d object detection," *CoRR*, vol. abs/1711.06396, 2017.
- [10] C. R. Qi, W. Liu, C. Wu, H. Su, and L. J. Guibas, "Frustum pointnets for 3d object detection from RGB-D data," *CoRR*, vol. abs/1711.08488, 2017.
- [11] A. Geiger, P. Lenz, and R. Urtasun, "Are we ready for autonomous driving? the kitti vision benchmark suite," in *Conference on Computer Vision and Pattern Recognition (CVPR)*, 2012.
- [12] K. He, X. Zhang, S. Ren, and J. Sun, "Deep residual learning for image recognition," *CoRR*, vol. abs/1512.03385, 2015.
- [13] T. Lin, P. Dollár, R. B. Girshick, K. He, B. Hariharan, and S. J. Belongie, "Feature pyramid networks for object detection," *CoRR*, vol. abs/1612.03144, 2016.
- [14] C. R. Qi, H. Su, K. Mo, and L. J. Guibas, "Pointnet: Deep learning on point sets for 3d classification and segmentation," *CoRR*, vol. abs/1612.00593, 2016.
- [15] C. R. Qi, L. Yi, H. Su, and L. J. Guibas, "Pointnet++: Deep hierarchical feature learning on point sets in a metric space," *CoRR*, vol. abs/1706.02413, 2017.
- [16] D. Eigen, C. Puhrsch, and R. Fergus, "Depth map prediction from a single image using a multi-scale deep network," *CoRR*, vol. abs/1406.2283, 2014.
- [17] P. K. Nathan Silberman, Derek Hoiem and R. Fergus, "Indoor segmentation and support inference from rgb-d images," in *ECCV*, 2012.
- [18] M. Sun, A. Y. Ng, and A. Saxena, "Make3d: Learning 3d scene structure from a single still image," *IEEE Transactions on Pattern Analysis & Machine Intelligence*, vol. 31, pp. 824–840, 05 2008.
- [19] B. Li, Y. Dai, H. Chen, and M. He, "Single image depth estimation by dilated deep residual convolutional neural network and soft-weight-sum inference," *CoRR*, vol. abs/1705.00534, 2017.
- [20] F. Yu and V. Koltun, "Multi-scale context aggregation by dilated convolutions," *CoRR*, vol. abs/1511.07122, 2015.
- [21] B. Li, Y. Dai, and M. He, "Monocular depth estimation with hierarchical fusion of dilated cnns and soft-weighted-sum inference," *CoRR*, vol. abs/1708.02287, 2017.
- [22] A. Mousavian, D. Anguelov, J. Flynn, and J. Kosecka, "3d bounding box estimation using deep learning and geometry," *CoRR*, vol. abs/1612.00496, 2016.
- [23] K. Simonyan and A. Zisserman, "Very deep convolutional networks for large-scale image recognition," *CoRR*, vol. abs/1409.1556, 2014.
- [24] Matterport, "Mask r-cnn for object detection and instance segmentation on keras and tensorflow." [https://github.com/matterport/Mask\\_RCNN](https://github.com/matterport/Mask_RCNN), 2017.
- [25] "3d object detection evaluation 2017." [http://www.cvlibs.net/datasets/kitti/eval\\_object.php?obj\\_benchmark=3d](http://www.cvlibs.net/datasets/kitti/eval_object.php?obj_benchmark=3d). Accessed: 2018-03-26.
- [26] "3d single-shot detector." [http://www.cvlibs.net/datasets/kitti/eval\\_object\\_detail.php?result=56b8c218bcd5eb69c1ad09cc43bd9e440084499a](http://www.cvlibs.net/datasets/kitti/eval_object_detail.php?result=56b8c218bcd5eb69c1ad09cc43bd9e440084499a). Accessed: 2018-03-26.
- [27] F. Liu, C. Shen, and G. Lin, "Deep convolutional neural fields for depth estimation from a single image," *CoRR*, vol. abs/1411.6387, 2014.
- [28] F. Liu, C. Shen, G. Lin, and I. D. Reid, "Learning depth from single monocular images using deep convolutional neural fields," *CoRR*, vol. abs/1502.07411, 2015.
- [29] S. R. Richter, Z. Hayder, and V. Koltun, "Playing for benchmarks," *CoRR*, vol. abs/1709.07322, 2017.
- [30] longcw, "Yolov2 in pytorch." <https://github.com/longcw/yolo2-pytorch>, 2017.
- [31] J. Yang and D. P. Jiasen Lu, Dhruv Batra, "A faster pytorch implementation of faster r-cnn." <https://github.com/jwyang/faster-rcnn.pytorch>, 2017.

## A. Estimating Translation

The supplementary material to the paper about Constrained Regression [22] explains how to obtain the translation of the 3D bounding boxes. The following equations are provided, which have been slightly adapted for comprehensibility:

$$\begin{aligned} \left( K \begin{bmatrix} I & R \times X_{\min} \\ 0 & 1 \end{bmatrix} \begin{bmatrix} T_x \\ T_y \\ T_z \\ 1 \end{bmatrix} \right)_{\tilde{x}} &= x_{\min} \\ \left( K \begin{bmatrix} I & R \times Y_{\min} \\ 0 & 1 \end{bmatrix} \begin{bmatrix} T_x \\ T_y \\ T_z \\ 1 \end{bmatrix} \right)_{\tilde{y}} &= y_{\min} \\ \left( K \begin{bmatrix} I & R \times X_{\max} \\ 0 & 1 \end{bmatrix} \begin{bmatrix} T_x \\ T_y \\ T_z \\ 1 \end{bmatrix} \right)_{\tilde{x}} &= x_{\max} \\ \left( K \begin{bmatrix} I & R \times Y_{\max} \\ 0 & 1 \end{bmatrix} \begin{bmatrix} T_x \\ T_y \\ T_z \\ 1 \end{bmatrix} \right)_{\tilde{y}} &= y_{\max} \end{aligned}$$

$K$  is the matrix containing the camera intrinsics:

$$K = \begin{bmatrix} \alpha_x & 0 & u_0 & 0 \\ 0 & \alpha_y & v_0 & 0 \\ 0 & 0 & 1 & 0 \end{bmatrix}$$

$R$  refers to the rotation matrix, which can be derived from the predicted angle.

$x_{\min}$ ,  $x_{\max}$ ,  $y_{\min}$ , and  $y_{\max}$  refer to the image coordinates of the horizontal and vertical edges of the 2D bounding boxes, whereas the uppercase version  $X_{\min}$ ,  $X_{\max}$ ,  $Y_{\min}$ , and  $Y_{\max}$  are the corners of the 3D bounding box that lie on these edges. Note that more than one corner can lie on the same edge, in which case the result will be the same regardless of which corner is used.

$T_x$ ,  $T_y$ , and  $T_z$  are the unknown translation parameters, which we want to find out in order to know where the object is located in 3D space.

The  $\tilde{x}$  and  $\tilde{y}$  indices after the parentheses indicate that a coordinate must be extracted from the homogeneous coordinate vector:

$$\left( \begin{bmatrix} x \\ y \\ z \end{bmatrix} \right)_{\tilde{x}} = \frac{x}{z} \quad \left( \begin{bmatrix} x \\ y \\ z \end{bmatrix} \right)_{\tilde{y}} = \frac{y}{z}$$

The supplementary material from [22] states that it is possible to convert these into a set of linear equations, but does not list these. As such, we calculated them:

$$\begin{bmatrix} -1 & 0 & \alpha_x^{-1}(x_{\min} - u) \\ 0 & -1 & \alpha_y^{-1}(y_{\min} - v) \\ -\alpha_x(u - x_{\max})^{-1} & 0 & -1 \\ 0 & -\alpha_y(v - y_{\max})^{-1} & -1 \end{bmatrix} \begin{bmatrix} T_x \\ T_y \\ T_z \end{bmatrix} = \begin{bmatrix} r_x^0 + \alpha_x^{-1}r_z^0(u_0 - x_{\min}) \\ r_y^1 + \alpha_y^{-1}r_z^1(v_0 - y_{\min}) \\ r_z^2 + \alpha_x r_x^2(u_0 - x_{\max})^{-1} \\ r_z^3 + \alpha_y r_y^3(v_0 - y_{\max})^{-1} \end{bmatrix}$$

where

$$\begin{bmatrix} r_x^0 & r_x^1 & r_x^2 & r_x^3 \\ r_y^0 & r_y^1 & r_y^2 & r_y^3 \\ r_z^0 & r_z^1 & r_z^2 & r_z^3 \end{bmatrix} = R \times \begin{bmatrix} X_{\min} & Y_{\min} & X_{\max} & Y_{\max} \end{bmatrix}$$

$T_x$ ,  $T_y$ , and  $T_z$  can now be found by using the least squares solution to this system of equations.

## B. Solving for $x$ and $y$ using offsets

Let  $K$  be the camera intrinsics matrix from equation (A) on the preceding page.

Let the 2D region of interest center be  $\begin{bmatrix} u \\ v \end{bmatrix}$ .

Let the 3D object center be  $\begin{bmatrix} x \\ y \\ z \end{bmatrix}$ .

### B.1. Solving for $x$ and $y$ using $du$ and $dv$

This method calculates the offset in image coordinates.

Let the projected 3D object center be  $\begin{bmatrix} u + du \\ v + dv \end{bmatrix}$ .

The relationship between camera and image coordinates is described by:

$$z \begin{bmatrix} u + du \\ v + dv \\ 1 \end{bmatrix} = K \begin{bmatrix} x \\ y \\ z \\ 1 \end{bmatrix}$$

Solving for  $x$  and  $y$  yields:

$$x = \frac{z}{\alpha_x} (u + du - u_0)$$
$$y = \frac{z}{\alpha_y} (v + dv - v_0)$$

### B.2. Solving for $x$ and $y$ using $dx$ and $dy$

This method calculates the offset in camera coordinates.

Let the transformed region of interest center be  $\begin{bmatrix} x + dx \\ y + dy \\ z \end{bmatrix}$ .

The relationship between camera and image coordinates is described by:

$$z \begin{bmatrix} u \\ v \\ 1 \end{bmatrix} = K \begin{bmatrix} x + dx \\ y + dy \\ z \\ 1 \end{bmatrix}$$

Solving for  $x$  and  $y$  yields:

$$x = \frac{z(u - u_0)}{\alpha_x} - dx$$
$$y = \frac{z(v - v_0)}{\alpha_y} - dy$$